Research Square

Preprints are preliminary reports that have not undergone peer review.
They should not be considered conclusive, used to inform clinical practice,
or referenced by the media as validated information.

Fatigue Behavior of Aerospace Titanium Alloy Ti-6Al-4V Samples Produced by 3D Electron Beam Melting Technology

Sviatoslav Motrunich

paton.testlab@gmail.com

E.O.Paton Electric Welding Institute https://orcid.org/0000-0002-8841-8609

Volodymyr Nesterenkov

Institut elektrozvaruvanna imeni E O Patona Nacional'na akademia nauk Ukraini

Illia Klochkov

Institut elektrozvaruvanna imeni E O Patona Nacional'na akademia nauk Ukraini

Vladyslav Matviichuk

Institut elektrozvaruvanna imeni E O Patona Nacional'na akademia nauk Ukraini

Maksym Tsysar

Institut elektrozvaruvanna imeni E O Patona Nacional'na akademia nauk Ukraini

Serhiy Akhonin

Institut elektrozvaruvanna imeni E O Patona Nacional'na akademia nauk Ukraini

Research Article

Keywords: Titanium Alloy, High-cyclic Fatigue, Additive Manufacturing, Electron Beam Additive Manufacturing, Mechanical Properties.

Posted Date: November 12th, 2026

DOI: https://doi.org/10.21203/rs.3.rs-11380930/v1

License: This work is licensed under a Creative Commons Attribution 4.0 International License.
Read Full License

XIII-3265-2026

Fatigue Behavior of Aerospace Titanium Alloy Ti-6Al-4V Samples Produced by 3D Electron Beam Melting Technology

Sviatoslav Motrunich*, Volodymyr Nesterenkov, Illia Klochkov, Vladyslav Matviichuk, Maksym Tsysar, Serhiy Akhonin

E.O. Paton Electric Welding Institute of NAS of Ukraine, Kyiv, Ukraine
*Corresponding author, paton.testlab@gmail.com

Abstract

This study investigates the fatigue behavior, tensile properties, and microstructural characteristics of Ti-6Al-4V (Grade 5) specimens produced by electron beam melting (EBM). Ti-6Al-4V is widely used in aerospace, rocketry, marine, and biomedical applications owing to its high specific strength, thermal stability, and corrosion resistance. The influence of key EBM process parameters on surface quality was established across 25 parameter combinations, and as-printed specimen density was determined by hydrostatic weighing. Microstructural homogeneity was assessed through Vickers hardness mapping and SEM analysis. High-cycle fatigue tests were conducted at a stress ratio of R_s = 0.1, and S-N curves were constructed and compared against reference data for conventionally produced Ti-6Al-4V. While the tensile strength of as-printed material (R_m = 959…974 MPa, δ = 6.5…8.5%) met or exceeded the requirements for annealed Grade 5 product forms, fatigue life was found to be significantly lower under the tested process conditions — fatigue limit $\Delta\sigma_{c,50\%}$ = 201 MPa at $2 \cdot 10^6$ cycles compared to 520 MPa for the reference material. Fractographic analysis by scanning electron microscopy identified inter-layer lack-of-fusion defects and clusters of unmelted powder particles as primary fatigue crack initiation sites, directly attributable to insufficient volumetric energy density at 100 µm layer thickness. The results demonstrate that satisfactory static strength is an insufficient qualification criterion for fatigue-critical EBM aerospace components, and that strict process parameter control is essential.

Keywords

Titanium Alloy, High-cyclic Fatigue, Additive Manufacturing, Electron Beam Additive Manufacturing, Mechanical Properties.

1. Introduction

Titanium alloys are currently critical materials in advanced engineering applications due to their high specific strength, corrosion resistance in atmospheric conditions, seawater and most aggressive environments [1]. They possess a range of other unique properties making them suitable for demanding applications that require reliable and long-lasting materials. Titanium alloys have found wide application in aerospace, shipbuilding, chemical engineering, and energy sectors. Among titanium alloys, Ti-6Al-4V (also designated as Grade 5 according to UNS R56400) stands out due combination of mechanical performance, biocompatibility, and versatility, making it the most widely used titanium alloy in aerospace, automotive, and biomedical engineering, accounting for more than 50% of total titanium alloy production worldwide [2].

Ti-6Al-4V is an two-phase (α+β) alloy belonging to the Ti-Al-V system (Table 1). The primary strengthening mechanisms involve solid solution strengthening by the α-stabilizing element aluminum and microstructural hardening through stabilization of the β-phase by vanadium [3]. The aluminum content provides significant strength and thermal stability, while

*

vanadium improves processability and ductility. The resulting alloy exhibits tensile strength typically in the range of 900…1100 MPa, yield strength of 830…970 MPa, and elongation of 10…15% depending on heat treatment condition [4].

Table 1 – Chemical composition and impurity limits of Ti-6Al-4V, wt%

Fe	C	Si	V	N	Ti	Al	Zr	O	H
<0,6	*<0,1*	*<0,1*	*3,5…5,3*	*<0,05*	*86,45…90,9*	*5,3…6,8*	*<0,3*	*<0,2*	*<0,015*

Ti-6Al-4V has excellent weldability for a high-strength titanium alloy. Standard heat treatment consists of annealing in the range of 700–850 °C to relieve residual stresses, followed by air or furnace cooling depending on the target microstructure. Solution treatment above the β-transus (~995 °C) followed by aging at 500…600 °C can be applied to achieve maximum strength [4, 5]. The alloy is extensively used in compressor blades, rotor discs, airframes, and fasteners in both commercial and military aircraft, with continuous service capability up to 300…350 °C.

Currently, Ti-6Al-4V semi-finished products are produced by vacuum arc remelting (VAR) of large-diameter ingots, followed by forging into smaller billets and subsequent rolling or extrusion. Obtaining high-quality titanium alloy ingots remains challenging due to the high sensitivity of titanium to interstitial impurities — particularly oxygen, nitrogen, hydrogen, and carbon — which form solid solutions or brittle compounds that degrade material quality. Electron beam cold hearth melting (EBCHM) is among the most effective vacuum metallurgy methods for producing titanium alloys with ultra-low content of dissolved gases, volatile impurities, and non-metallic inclusions. EBCHM allows independent control of the melting rate through adjustment of beam power, enabling precise control of melt superheating duration and near-complete removal of both high- and low-density refractory inclusions, substantially enhancing ingot quality [6, 7].

Most Ti-6Al-4V aerospace components are geometrically complex and expensive to produce by traditional subtractive methods due to extensive machining and high buy-to-fly ratios that can exceed 10:1. The advent of additive manufacturing (AM) and 3D printing technologies has fundamentally expanded the production potential of titanium alloys [8]. The ability to build parts directly from digital CAD models not only reduces material waste but also enables rapid prototyping and near-net-shape production of intricate geometries that are impossible or uneconomical by conventional means [9].

Among AM processes for titanium alloys, wire and arc additive manufacturing (WAAM) has been developed as a highly efficient technique for large-scale components. However, metal deposition by WAAM produces coarse columnar texture and anisotropic mechanical properties, which limits its application in fatigue-critical structures [10]. Powder bed fusion processes, and in particular electron beam melting (EBM), offer superior microstructural control through the combination of a vacuum processing environment and elevated build-chamber temperature, which suppress residual stress accumulation and oxidation — critical advantages for reactive titanium alloys [11].

The fatigue behavior of EBM Ti-6Al-4V is strongly governed by process-induced defects, particularly subsurface porosity and lack-of-fusion between adjacent melt tracks or layers. These defects act as stress concentrators and fatigue crack initiation sites, making fatigue life highly sensitive to the applied process parameters. While the static tensile properties of EBM Ti-6Al-4V can match or exceed those of conventionally produced material, fatigue performance is known to be more variable and process-dependent [12, 13]. Understanding this relationship between process parameter set and fatigue behavior is therefore essential for qualifying EBM components for safety-critical aerospace applications.

The main aim of this work is to investigate the high-cycle fatigue behavior of 3D-printed Ti-6Al-4V (Grade 5) titanium alloy produced by EBM technology and to compare it with reference data for conventionally produced Ti-6Al-4V [12], with particular attention to the role of process parameters and defect morphology on fatigue life.

2. Manufacturing technology and testing procedure

Ti-6Al-4V (Grade 5) powder for EBM printing was produced by plasma melting and centrifugal spraying (PREP technology). The powder particles exhibit regular spherical morphology with particle sizes ranging from 16.7 to 151.9 µm (mean ~95 µm), with the dominant fraction in the 100–160 µm range (52.2 wt.%). The chemical composition, verified by X-ray fluorescence (XRF) analysis using an Expert CUBE spectrometer (Helmut Fischer, Germany) gives Al = 5.53 wt.%, V = 4.33 wt.%, Fe = 0.10 wt.%, Si = 0.06 wt.%.

EBM printing was performed on experimental equipment (Figure 1) developed at the E.O. Paton Electric Welding Institute, described in detail in [17, 18]. The equipment consists of a vacuum chamber (640×640×640 mm internal dimensions), an electron beam gun, control cabinets, and a high-voltage power supply. The build zone dimensions are 200×200×180 mm. Maximum beam power is 6 kW, minimum beam diameter 0.2 mm, and maximum beam travel speed 300 mm/s. Working pressure in the vacuum chamber during printing was ~10^{-2} Pa. The accelerating voltage of the electron beam gun was 60 kV. Preheating of the powder layer was carried out with a raster beam at a power of 1900

W, maintaining the powder bed temperature at approximately 680 °C throughout the build. The scanning strategy was bidirectional with 90° layer-by-layer rotation; beam step offset was 0.2 mm; powder layer thickness was 0.1 mm. Two outer contour passes were applied to improve surface quality and dimensional stability of the side walls.



Figure 1 – Experimental equipment for electron beam additive manufacturing developed by E.O. Paton Electric Welding Institute: 1 – vacuum chamber; 2 – electron beam gun; 3 – control cabinets; 4 – high-voltage source

The technological parameters for EBM printing of Ti-6Al-4V were established in prior work [19, 20], where the influence of energy density and beam speed on surface quality, geometrical compliance, and microstructural homogeneity was systematically investigated across 25 parameter combinations at beam speeds of 500–12,000 mm/s and energy densities of 7.0–45.0 J/mm³. Three batches of prismatic specimens (25×25×7.5 mm, including 2.5 mm technological supports) were printed — 75 specimens total. After printing, the build assembly was gradually cooled in vacuum to approximately 200°C over six hours, a controlled thermal history that resembles a stress-relief anneal and promotes microstructural stabilization [4].

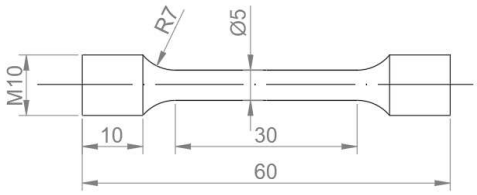
Microstructural characterization was performed on transverse cross-sections prepared by electrical discharge machining, followed by sequential grinding with abrasive paper, diamond suspension polishing, and chemical etching in an aqueous solution of 6% HNO_3 and 2% HF. Optical microscopy was performed on a Carl Zeiss Jena instrument in reflected light. Scanning electron microscopy (SEM) was carried out on a TESCAN VEGA 3 SBH EP at 20 kV in secondary electron (SE) and backscattered electron (BSE) modes to characterize grain morphology, porosity, and phase contrast. Chemical composition and elemental distribution were determined by XRF using a Bruker Quantax 610M spectrometer on polished cross-sections, covering atomic numbers Z = 12–92. Phase analysis was conducted by X-ray diffraction (XRD) on an Inel EQUINOX-1000 diffractometer in grazing incidence geometry (5° incidence angle), Cu Kα radiation (λ = 0.15418 nm), 2θ range 10–110°, operated at 30 kV / 15 mA; phase identification was performed using Match! software. Microhardness was measured by the Vickers method on a PMT-3 instrument at a load of 0.1 kgf (0.98 N) with 10 s dwell time, on polished cross-sections at three characteristic zones: center, layer boundaries, and near-surface region. α-phase crystal dimensions were measured from SEM images according to the methodology described in [23]. Based on this study the suitable regime was selected and batch of 18 samples 10x10x70 was manufactured for mechanical and fatigue testing.

Surface roughness of the as-printed specimens was measured using a JD-520 profilometer (Republic of Korea) with a traverse length of 5000 µm and step of 25.4 µm. The measured values were: Rt = 322–647 µm, Rz = 226–624 µm, Ra = 19–28 µm, confirming a highly developed as-built surface with height variation approaching 1 mm, characteristic of EBM parts prior to machining. Density of the as-printed specimens was determined by hydrostatic weighing using an AS220.R2 analytical balance (RadWag, Poland, Class 4) with distilled water as the immersion liquid at 21.8–22.4 °C. Measured density ranged from 4363 to 4395 kg/m³ with a standard deviation of 9.32 kg/m³, confirming high structural homogeneity across the print field.

For mechanical testing, proportional 5× cylindrical specimens (Figure 2b) were machined from the prismatic blanks in accordance with ISO 6892-1:2019: diameter 6 mm, gauge length 25 mm, lateral surface roughness Ra < 1.25 µm. Tensile testing was performed on an MTS 318.25 servohydraulic machine (250 kN capacity) at an initial crosshead speed of 2 mm/min through the elastic and yield region, increasing to 5 mm/min after yield, using an extensometer with 25 mm gauge length. Young's modulus was determined from the linear portion of the stress-strain curve in the 500–800 MPa stress range to avoid extensometer seating artefacts at low loads.



a



b

1	2	3	4	5	6	7	8	9
10	11	12	13	14	15	16	17	18

c

Figure 2 –3D printed sample (a), geometry of specimens (b) both for tensile and fatigue testing and general testing scheme of manufactured batch (c): #1,5,9 – tensile testing, #4,6,10-18 fatigue testing.

Fatigue specimens with polished gauge sections were machined to the geometry described in [21] (Figure 2b). Fatigue testing was performed according to ISO 1099 under force-controlled loading at stress ratio R_s = 0.1 and loading frequency of 20 Hz on the MTS 318.25 machine, either to total fracture or to runout at $2 \cdot 10^6$ cycles. S-N curves for constant amplitude loading were constructed from the test results. It should be noted that machining of fatigue specimens from the printed blanks redistributes or releases residual stresses induced during the EBM process; the fatigue results therefore represent intrinsic material behavior independent of the original print residual stress state [22].

Fracture surfaces of failed fatigue specimens were examined by SEM on a TESCAN MIRA3 at 20 kV accelerating voltage (SE detector, working distance ~33–36 mm) to identify crack initiation sites, defect morphology, and fracture mode.

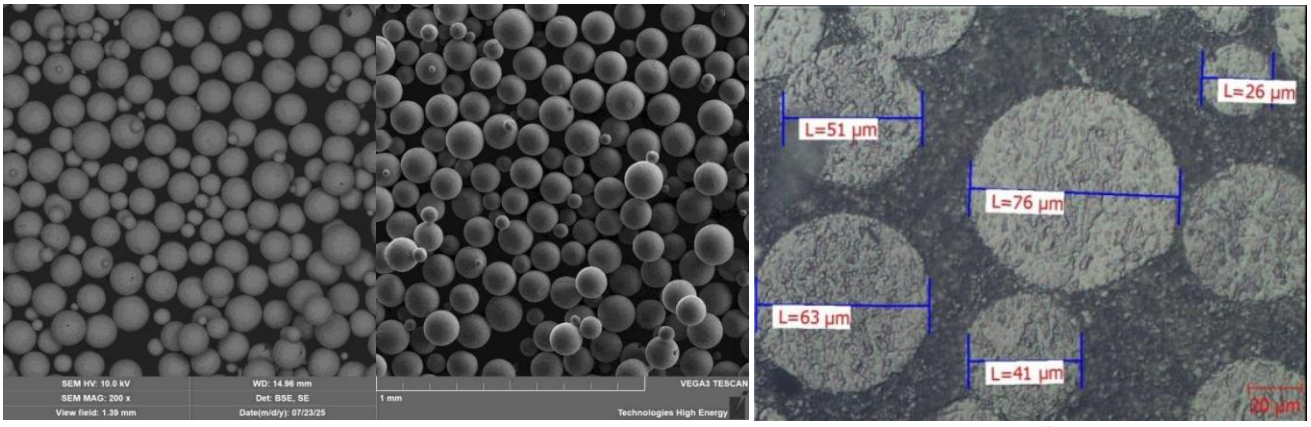
3. Results and discussion

3.1. Powder and as-printed specimen characterization

Ti-6Al-4V (Grade 5) powder produced by PREP technology was characterized prior to printing. SEM analysis confirmed that the powder particles exhibit regular spherical morphology with smooth surfaces and no visible agglomeration or satellite particles (Figure 3). The particle size distribution ranged from 16.7 to 151.9 µm with a mean of ~95 µm, with the dominant fraction in the −160+100 µm range (52.2 wt.%, Table 2).

Table 2 – Particle size distribution of Ti-6Al-4V (Grade 5) powder

Fraction Size		(wt.%)			
Min-max (µm)	Mean (µm)	−160+100	−100+63	−63+20	−20
16.7–151.9	94.97	52.2	25.46	22.16	0.18



a b

Figure 3 – SEM image (a) and dimensions (b) of Ti-6Al-4V (Grade 5) powder manufactured by PREP technology

To select proper EBM process parameters, three batches of 25 prismatic specimens (25×25×7.5 mm) were printed under systematically varied beam speeds (500–12,000 mm/s), energy densities (7.0–45.0 J/mm³), and dynamic focus currents (0–1.39 A) — 25 parameter combinations in total.Three surface morphology types were identified: smooth, bumpy,

and porous (Figure 4)— with smooth morphology obtained within specific energy density windows for each beam speed. Smooth morphology, associated with complete inter-layer fusion and minimal surface irregularity, was obtained within specific energy density windows at each beam speed [19, 20]. Based on these findings, a process parameters set was selected for all subsequent mechanical testing: beam speed 4000 mm/s, power 1750 W, energy density 22 J/mm³. Eighteen specimens were printed at this regime and used for microstructural characterization, tensile testing, and fatigue testing (Figure 2). Surface roughness of the as-printed screening specimens ranged from Rt = 322–647 µm, Rz = 226–624 µm, Ra = 19–28 µm, and density from 4363 to 4395 kg/m³ (mean 4378 kg/m³, relative density ~98.8%), confirming the absence of gross porosity across the print field.



a b c

Figure 4 – Different surface morphology types: porous (a), smooth (b) and bumpy (c)

3.2. Microstructure analysis

Chemical composition of printed specimens at the selected regime (4000 mm/s, 1750 W, 22 J/mm³) was verified by XRF analysis (Bruker Quantax 610M). Results confirmed conformity to Ti-6Al-4V (Grade 5) specification requirements: Al = 5.88–6.09 wt.%, V = 3.97–4.02 wt.%, Fe ≤ 0.14 wt.%, Si ≤ 0.05 wt.%. The uniform elemental distribution confirms the absence of significant evaporative loss of alloying elements under vacuum processing conditions.

Phase analysis by XRD (Inel EQUINOX-1000, Cu Kα, grazing incidence geometry) confirmed the predominance of hexagonal α-Ti phase with a minor β-Ti contribution. No oxide phases were detected, confirming chemical purity under vacuum processing conditions.

SEM and optical microscopy revealed the lamellar-columnar morphology characteristic of EBM-processed Ti-6Al-4V (Figure 5). Prior-β grains are elongated along the build direction, reflecting the steep thermal gradient inherent to the process. Within the columnar grains, a fine acicular and lamellar α-phase dominates, with thin interlath β-phase layers visible at higher magnification. Local zones of martensitic α'-phase are present at grain boundary regions, formed by rapid cooling from above the β-transus with partial back-transformation during subsequent layer reheating cycles.

The mean α-phase crystal size at the selected regime, measured from SEM images according to [23], ranged from 1.07 to 1.40 µm with maximum values of 2.05–3.21 µm. This fine-grained structure is attributable to the relatively high beam speed (4000 mm/s) and moderate energy density (22 J/mm³), which limit melt pool size and promote rapid solidification. For comparison, specimens printed at lower beam speeds and higher energy densities showed coarser lamellar colonies with mean α-crystal sizes of 2.2–4.2 µm — confirming the strong sensitivity of microstructure to EBM process parameters.

Vickers microhardness (HV0.1) measured across specimen cross-sections at the selected regime showed mean values of 409–434 kgf/mm² with a characteristic gradient along the build height. The near-surface zone exhibits elevated hardness (~490–540 kgf/mm²) correlated with fine α'-phase formation during rapid cooling of the final deposited layers. The mid-section shows mean values (470–540 kgf/mm²) reflecting repeated thermal cycling from subsequent layer depositions, while the lower zone exhibits slightly reduced hardness corresponding to the more stabilized α+β structure. This hardness gradient confirms the structural anisotropy inherent to layer-by-layer EBM deposition and is consistent with the fine α-crystal sizes measured at this regime.

3.3. Tensile mechanical testing

The as-printed EBM specimens exhibited Young's modulus E = 110…120 GPa, yield strength $R_{o.2}$ = 847…877 MPa, ultimate tensile strength R_m = 959…974 MPa, and elongation A = 6.5…8.5%. These values meet or exceed the requirements for all standard annealed Grade 5 product forms: tensile strength surpasses the minimum requirement for annealed rod (Table 3)

by 9–16%, while elongation equals or exceeds the corresponding ductility requirements (A ≥ 6–8%). Compared to the quench-and-aged condition (R_m ≥ 1080 MPa, A ≥ 4% per UNS R56400), the EBM material shows lower tensile strength but substantially superior ductility — elongation exceeding the quench-and-aged minimum by more than 85% — making it particularly suitable for components where damage tolerance is critical.

Table 3 –Mechanical properties of EBM Ti-6Al-4V compared to ASTM and UNS R56400 standard values

Material condition	Young`s modulus E (GPa)	Yield stress $R_{0.2}$ (MPa)	Ultimate stress R_m (MPa)	Elongation A (%)	Area Reduction Z (%)
EBM Ti-6Al-4V (this work)	110–120	847–877	959–974	6,5…8,5	15…20
Annealed rod	110-115	—	835–885	≥6…8	15…20
Rod premium quality			835–1050	≥6…10	20
Quench + aged rod			≥1080	≥4	12
Annealed plate			835–1080	≥6	12…16

The favorable combination of strength and ductility in the as-printed condition, without any post-process heat treatment, is attributed to the in-situ thermal cycle inherent to the EBM process. Maintenance of the powder bed at approximately 680 °C throughout the build, followed by controlled slow cooling in vacuum, effectively constitutes a stress-relief anneal that promotes decomposition of the metastable martensitic α'-phase into a stable fine-grained α+β microstructure [4, 5]. This thermally induced microstructural stabilization is reflected in the stress-strain curves Figure 5 a, which exhibit a well-defined elastic region, smooth yield transition without a pronounced yield drop, and an extended plastic plateau at 930–974 MPa spanning strains of 1–6% — behavior characteristic of a well-annealed two-phase titanium alloy with good strain homogeneity and no Portevin–Le Chatelier instability.

3.4. High cyclic fatigue behavior

S-N curves for EBM Ti-6Al-4V and wrought/forged Ti-6Al-4V reference data [12] at R_s = 0.1 are presented in Figure 5. The statistical parameters derived from constant amplitude test results are summarized in Table 4.

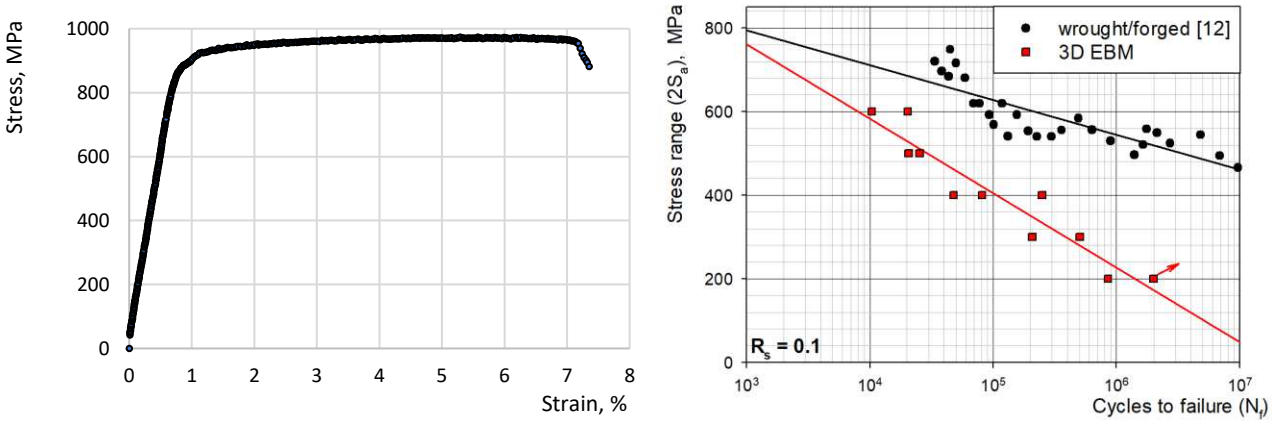


Figure 5 – Stress-strain curve and S-N curve of EBM 3D printed Ti-6Al-4V titanium alloy samples

The wrought/forged Ti-6Al-4V reference exhibits a shallow S-N slope (m = 16.4) with a fatigue limit at $2 \cdot 10^6$ cycles of $\Delta\sigma_{c,50\%}$ = 520 MPa and $\Delta\sigma_{c,95\%}$ = 466 MPa, consistent with literature data for conventionally produced material [12, 13]. The EBM specimens demonstrate a significantly steeper S-N curve (m = 4.7), with fatigue limit Δσc,50% = 201 MPa and Δσc,95% = 164 MPa at $2 \cdot 10^6$ cycles — a reduction of approximately 61% relative to the wrought/forged reference at 50% failure probability. The higher scatter ratio of the EBM data (T_σ = 1.51, Slog = 0.055) compared to the wrought/forged reference (T_σ = 1.24, S_{log} = 0.029) reflects the stochastic nature of internal defect distributions inherent to the tested process parameter combination.

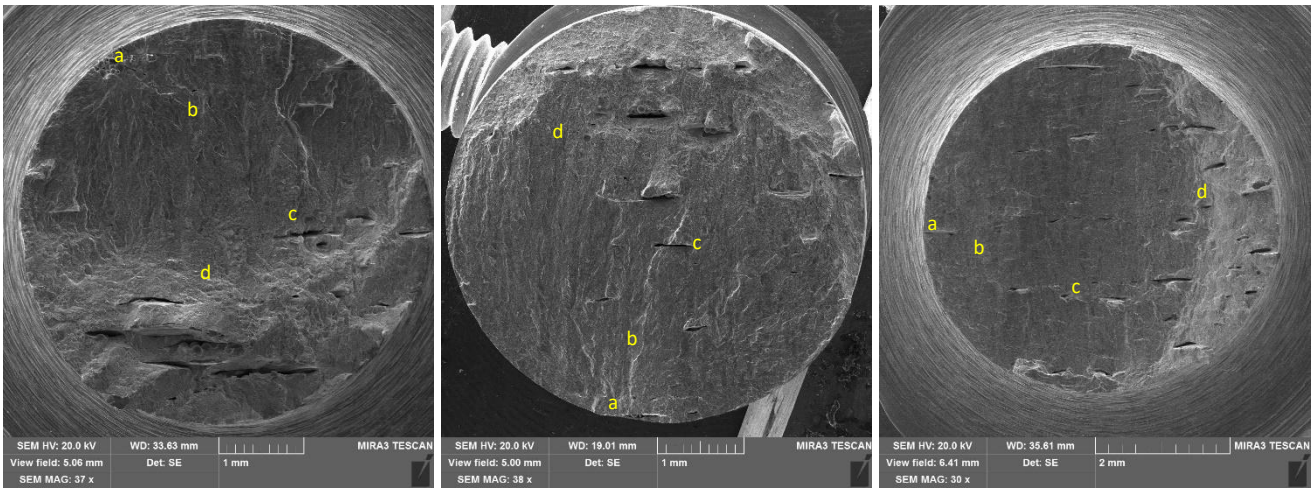
Table 4 – Fatigue data

Ti-6Al-4V	Free slope, m	S_{log}	Scatter ratio, T_σ	$\Delta\sigma_{c,50\%}$ at $2{\cdot}10^6$ (MPa)	$\Delta\sigma_{c,95\%}$ at $2{\cdot}10^6$ (MPa)
EBM (this work)	4.7	0.055	1.51	201	164
wrought/forged [12]	16.4	0.029	1.24	520	466

The steep S-N slope is characteristic of defect-controlled fatigue failure, where crack initiation life is governed by internal defects rather than microstructural features. This contrasts with the shallow slope of the wrought/forged reference, which is typical of microstructure-controlled crack initiation. Notably, despite EBM tensile strength meeting or exceeding ASTM annealed rod requirements (Section 3.3), fatigue performance is severely degraded — demonstrating that static strength alone is an insufficient qualification criterion for fatigue-critical aerospace components produced by additive manufacturing. The fractographic evidence supporting this interpretation is presented in Section 3.5.

3.5. Fractographic analysis

SEM examination of fracture surfaces revealed a consistent defect-controlled failure mechanism across all tested stress amplitudes (Figure 6). In all three examined specimens, fatigue crack initiation occurred at lack-of-fusion defects located at or immediately beneath the specimen surface — not at microstructural features such as grain boundaries or α/β interfaces as would be expected for optimally processed EBM material. Two morphologically distinct defect types were identified. At higher stress amplitudes, crack initiation occurred at clusters of unmelted spherical powder particles (50…100 µm diameter) trapped within inter-layer voids, recognizable by their perfect spherical morphology and complete absence of metallurgical bonding to the surrounding matrix (Figure 7a,b). At lower stress amplitudes, initiation sites were dominated by pure inter-layer lack-of-fusion voids of elongated planar geometry — aspect ratio exceeding 10:1, oriented parallel to the build plane — with one smooth unbonded layer surface and one fractured face (Figure 7c). Both defect types share a common process origin: insufficient volumetric energy density for complete inter-layer fusion at 100 µm layer thickness, resulting in either incomplete powder melting or partial inter-layer bonding.

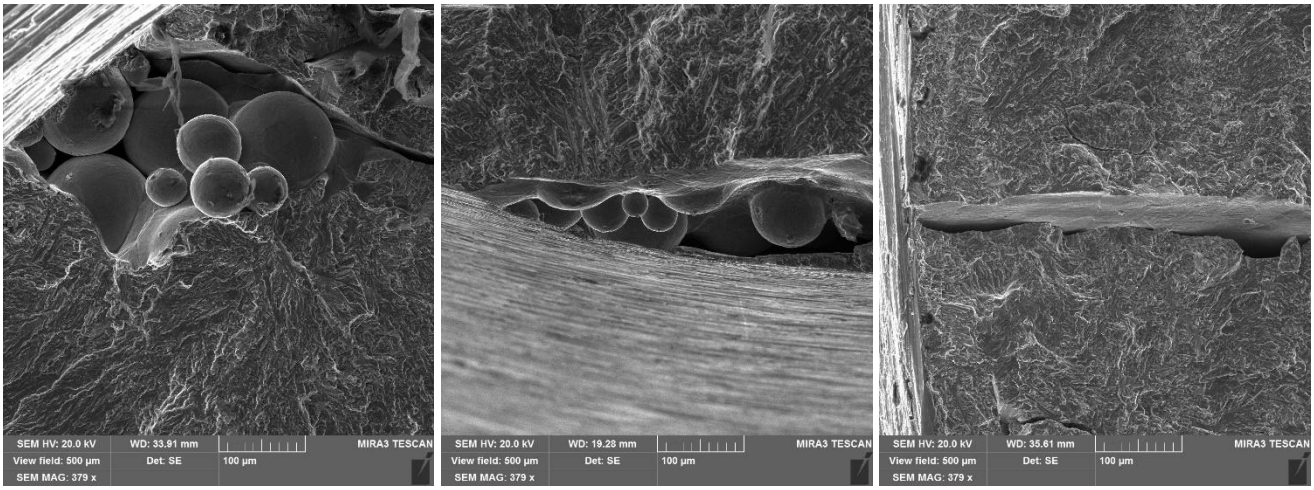


a b c

Figure 6 – Fracture surface overview of EBM Ti-6Al-4V fatigue specimens at R_s = 0.1: (a) 500 MPa / 20,658 cycles; (b) 300 MPa / 207,120 cycles; (c) 200 MPa / 853,979 cycles. Zones: a — crack initiation site; b — fatigue crack propagation zone; c — stable propagation with distributed lack-of-fusion defects; d —fracture zone. Note progressive increase of propagation zone with decreasing stress amplitude.

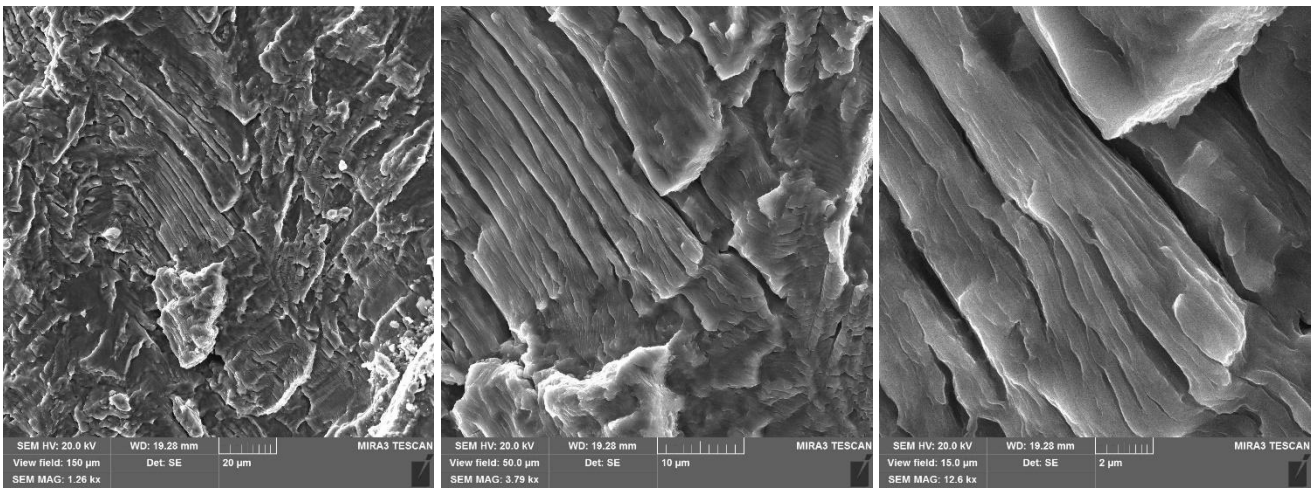
A systematic evolution of fracture zone proportions with applied stress was observed across specimens. As stress amplitude decreased from 500 to 200 MPa, the fatigue crack propagation zone expanded from approximately 65% to 83% of the cross-sectional area, while the fast fracture zone contracted correspondingly. Fatigue striations were resolved at intermediate stress (300 MPa) with a spacing of approximately 0,3…0,5 µm, confirming stable cyclic crack advance through the lamellar α+β microstructure (Figure 8). In addition to initiation-site defects, distributed inter-layer lack-of-fusion voids were present throughout the cross-sections of all specimens — more than 20 individual voids countable at low magnification in the lowest-stress specimen — acting as secondary crack accelerators during propagation and contributing to the elevated scatter ratio (T_σ = 1.51) observed in the S-N data. The characteristic planar geometry and smooth unbonded surfaces of

these voids unambiguously identify them as inter-layer lack-of-fusion defects (Figure 7), directly attributable to the applied process parameter combination. Reducing the powder layer thickness to 50…75 µm is expected to increase energy penetration depth, suppress inter-layer disbonding, and eliminate unmelted particle clusters, with a corresponding improvement in fatigue performance toward values reported for optimized EBM Ti-6Al-4V in the literature [13, 14].



a b c

Figure 7 –Crack initiation defects in EBM Ti-6Al-4V: (a) cluster of unmelted spherical powder particles at near-surface lack-of-fusion void, Specimen #1, 379×; (b) tilted view revealing planar three-dimensional geometry of inter-layer lack-of-fusion void with entrapped particles, Specimen #2, 379×; (c) elongated inter-layer lack-of-fusion void in plain view showing smooth unbonded layer surface, Specimen #3, 379×. Scale bars 100 µm



a b c

Figure 8 – Example of fatigue crack propagation zone for Specimen #2 (300 MPa, 207,120 cycles): (a) lamellar transgranular fracture morphology in propagation zone (1.26 kx); (b) transition zone showing mixed cleavage and fatigue features (3.79 kx); (c) fatigue striations confirming stable cyclic crack advance, striation spacing 0,3…0,5 µm (12.6 kx)

4. Conclusions

1. EBM Ti-6Al-4V (Grade 5) powder produced by PREP technology exhibited regular spherical morphology, chemical composition, and high batch homogeneity confirmed by as-printed specimen density of 4363–4395 kg/m³ (relative density ~98.8%). These powder and process characteristics are suitable for the production of aerospace structural components.

2. The as-printed EBM Ti-6Al-4V material, without post-process heat treatment, achieved tensile strength R_m = 959…974 MPa, yield strength $R_{0,2}$ = 847…877 MPa, Young's modulus E = 110…120 GPa, and elongation δ = 6.5…8.5%, meeting or exceeding the requirements for annealed Grade 5 rod and plate product forms per UNS R56400 and ASTM standards. The favorable strength-ductility balance is attributed to the in-situ stress-relief annealing effect

of the EBM thermal cycle — powder bed preheating at 680°C and controlled vacuum cooling — which promotes decomposition of metastable α'-martensite into a stable fine-grained α+β microstructure.

3. High-cycle fatigue testing at $R_s = 0.1$ revealed that EBM Ti-6Al-4V specimens produced under the tested parameter combination exhibit a fatigue limit at $2 \cdot 10^6$ cycles of $\Delta\sigma_{c,50\%} = 201$ MPa — a reduction of approximately 61% compared to wrought/forged Ti-6Al-4V reference data ($\Delta\sigma_{c,50\%} = 520$ MPa). The S-N curve slope m = 4.7 is significantly steeper than that of the wrought/forged reference (m = 16.4), and the scatter ratio $T_\sigma = 1.51$ is elevated, both characteristic of defect-controlled fatigue failure. These results demonstrate that satisfactory static strength is insufficient as a sole qualification criterion for fatigue-critical EBM components.

4. Fractographic analysis identified lack-of-fusion defects as the exclusive crack initiation sites across all tested stress amplitudes. Two defect types were observed: clusters of unmelted spherical powder particles at near-surface inter-layer voids, and pure inter-layer lack-of-fusion disbonds of elongated planar geometry with aspect ratio exceeding 10:1, oriented parallel to the build plane. Both defect types originate from insufficient volumetric energy density for complete inter-layer fusion at 100 µm layer thickness. Fatigue striations confirmed stable cyclic crack propagation through the lamellar α+β microstructure prior to final fracture.

5. Reduction of powder layer thickness to 50…75 µm is expected to increase energy penetration depth per layer, suppress inter-layer lack-of-fusion defect formation, and eliminate unmelted powder particle clusters, with a corresponding improvement of fatigue performance toward literature values reported for optimized EBM Ti-6Al-4V. This will be the subject of future investigation.

5. Funding and/or Conflicts of interests/Competing interests

This research was funded under the state budget program "Support for the Development of Priority Areas of Scientific Research" (CPCEB 6541230). The authors declare that no conflict of interest or competing interest exist with regard to the scope of this article.

6. Data Availability Statement

The authors declare that the data supporting the findings of this study are available within the paper.

7. Authors Contributions

All authors contributed to the study through the roles described below. **S. Motrunich:** Conceptualization, Methodology (experimental design), Investigation (mechanical and fatigue testing), Formal analysis (fatigue and fracture behavior), Writing – original draft. **V. Nesterenkov:** Supervision (electron beam additive manufacturing), Resources. **I. Klochkov:** Methodology (testing program and specimen design), Supervision, Project administration, Writing – review & editing. **V. Matviichuk:** Methodology (EBM process development), Investigation (manufacturing of test blanks). **M. Tsysar:** Investigation (material characterization), Data curation, Visualization. **S. Akhonin:** Supervision (overall scientific guidance), Project administration (research coordination). All authors contributed to the discussion and interpretation of the results and critically reviewed the manuscript. All authors read and approved the final manuscript.

8. References

[1] Zhao D. (2014) Development and Application of Titanium Alloys in the Aviation. Foundry 63(11):114–117
[2] Leyens C., Peters M. (eds.) (2003) Titanium and Titanium Alloys: Fundamentals and Applications. Wiley-VCH, Weinheim. ISBN 978-3-527-30534-6
[3] Donachie M.J. (2000) Titanium: A Technical Guide, 2nd ed. ASM International, Materials Park OH. ISBN 978-0-87170-686-7
[4] Lütjering G., Williams J.C. (2007) Titanium, 2nd ed. Springer, Berlin. DOI: 10.1007/978-3-540-71398-2
[5] in J.J., Lv Y.H., Liu Y.X., Xu B.S., Sun Z., Li Z.G., Wu Y.X. (2016) Microstructural evolution and mechanical properties of Ti-6Al-4V wall deposited by pulsed plasma arc additive manufacturing. Materials and Design 102:30 – 40. DOI: 10.1016/j.matdes.2016.04.018

[6] Akhonin S.V., Mishchenko R.N., Petrichenko I.K. (2006) Investigation of the weldability of titanium alloys produced by different methods of melting. Materials Science 42(3):323–329. DOI: 10.1007/s11003-006-0088-9
[7] Akhonin S., Berezos V., Severyn A., Gadzyra M., Tymoschenko Y., Davydchuk N. (2019) Structure and Properties of Titanium Modified Silicon-carbide at EBCHM. IOP Conference Series: Materials Science and Engineering 582:012051. DOI: 10.1088/1757-899X/582/1/012051
[8] Ran J., Jiang F., Chen Z., Zhao H. (2022) Microstructure and Mechanical Properties of TA15 Alloy Produced by Electron Beam Melting. Metals and Materials International 27(3):770–786. DOI: 10.1007/s12540-019-00536-0
[9] Huang S., Sun B., Guo S. (2021) Microstructure and property evaluation of TA15 titanium alloy fabricated by selective laser melting after heat treatment. Optics and Laser Technology 144:107422. DOI: 10.1016/j.optlastec.2021.107422
[10] Yu Z., Yu S., Yu G., Fu M.W. (2024) Correlation between pulse frequencies, microstructure and mechanical properties of TA15 in wire and arc additive manufacturing. Journal of Materials Research and Technology 30:7621–7634. DOI: 10.1016/j.jmrt.2024.05.149
[11] Murr L.E., Gaytan S.M., Ramirez D.A., Martinez E., Hernandez J., Amato K.N., Shindo P.W., Medina F.R., Wicker R.B. (2012) Metal fabrication by additive manufacturing using laser and electron beam melting technologies. Journal of Materials Science and Technology 28(1):1–14. DOI: 10.1016/S1005-0302(12)60016-4
[12] Wang K., Wang F., Cui W., Hayat T., Ahmad B. (2014) Prediction of short fatigue crack growth of Ti-6Al-4V. Fatigue & Fracture of Engineering Materials & Structures 37(10):1075–1086. DOI: 10.1111/ffe.12177
[13] Leuders S., Thöne M., Riemer A., Niendorf T., Tröster T., Richard H.A., Maier H.J. (2013) On the mechanical behaviour of titanium alloy TiAl6V4 manufactured by selective laser melting: Fatigue resistance and crack growth performance. International Journal of Fatigue 48:300–307. DOI: 10.1016/j.ijfatigue.2012.11.011
[14] Wycisk E., Solbach A., Siddique S., Herzog D., Walther F., Emmelmann C. (2015) Effects of defects in laser additive manufactured Ti-6Al-4V on fatigue properties. Physics Procedia 56:371–378. DOI: 10.1016/j.phpro.2014.08.120
[15] Gong H., Rafi K., Gu H., Starr T., Stucker B. (2015) Analysis of defect generation in Ti–6Al–4V parts made using powder bed fusion additive manufacturing processes. Additive Manufacturing 1–4:87–98. DOI: 10.1016/j.addma.2014.08.002
[16] Tammas-Williams S., Zhao H., Léonard F., Derguti F., Todd I., Prangnell P.B. (2015) XCT analysis of the influence of melt strategies on defect population in Ti–6Al–4V components manufactured by Selective Electron Beam Melting. Materials Characterization 102:47–61. DOI: 10.1016/j.matchar.2015.02.008
[17] Matviichuk V.A., Nesterenkov V.M., Berdnikova O.M. (2022) Additive electron beam technology of manufacture of metal products from powder materials. The Paton Welding Journal 2:16–25. DOI: 10.37434/tpwj2022.02.03
[18] Akhonin S., Nesterenkov V., Pashynskyi V., Matviichuk V., Motrunich S., Berezos V., Klochkov I. (2024) Determining technological parameters for obtaining TA15 titanium alloy blanks with improved mechanical characteristics using the electron-beam 3D printing method. Eastern-European Journal of Enterprise Technologies 3(12/129):36–45. DOI: 10.15587/1729-4061.2024.306613
[19] Tsysar M.O., Klochkov I.M., Motrunich S.I., Katok O.A., Matviichuk V.A., Babak A.M. (2024) Principles of additive electron beam technology for manufacturing spare parts from VT20 titanium alloy powder. Tooling Materials Science 26(1):331–346
[20] Akhonin S., Pikulin O., Berezos V., Severyn A., Erokhin O., Kryzhanovskyi V. (2022) Determining the structure and properties of heat-resistant titanium alloys VT3-1 and VT9 obtained by electron-beam melting. Eastern-European Journal of Enterprise Technologies 5(12/119):6–12. DOI: 10.15587/1729-4061.2022.265014
[21] Motrunich S., Berezos V., Kostin V., Klochkov I., Akhonin D. (2024) Fatigue behavior and fracture of medical Ti-6Al-7Nb titanium alloy produced by electron beam cold hearth melting. Procedia Structural Integrity 56:155–162. DOI: 10.1016/j.prostr.2024.04.010
[22] Nesterenkov V., Akhonin S., Klochkov I., Matviichuk V., Berezos V., Motrunich S. (2025) High cyclic fatigue behavior of 3D-printed titanium alloy TA15. Welding in the World. DOI: 10.1007/s40194-025-01945-3
[23] Weiss I., Froes F.H., Eylon D. et al. (1986) Modification of alpha morphology in Ti-6Al-4V by thermomechanical processing. *Metallurgical Transactions A* 17:1935–1947. DOI: 10.1007/BF02644991